

# A hindrance-plane-hindrance molecular engineering strategy towards self-assembled nanorods for enhanced photodynamic therapy

Received: 10 June 2025

Accepted: 6 November 2025

Published online: 21 November 2025

Check for updates

Qiaoyang Tang <sup>1</sup>, Binghui Xue <sup>2</sup>, Hanyu Jia<sup>1</sup>, Yubo Liu<sup>1</sup>, Ben Zhong Tang <sup>3</sup> & Guangxue Feng <sup>1</sup> ✉

As the vital component of photodynamic therapy, organic photosensitizers face challenges in clinical translation due to their compromised reactive oxygen species generation and limited tumor targeting when aggregated or formulated as nanoparticles. Herein, we overcome this dilemma by proposing a steric hindrance–plane–hindrance molecular design strategy to guide the self-assembly of twisted donor– $\pi$ –acceptor photosensitizers into rod-shaped nanoparticles, which concurrently enhance reactive oxygen species (ROS) generation and tumor accumulation. Using TPA-S-DCR and other 7 molecules as models, we demonstrate that tuning the donor and acceptor steric hindrances around  $\pi$ -conjugated planar center enables the controllable spherical or rod-shaped supramolecular self-assembly of these twisted donor– $\pi$ –acceptor photosensitizers under mild sonication condition. The resulting nanorods exhibit 1.31-fold higher ROS production, 5.04-fold higher cancer cell uptake over the nano-spherical counterparts. Moreover, TPA-S-DCR nanorods also show higher tumor accumulation, deeper tumor penetration, and longer tumor retention over its nano-spherical counterpart, which together with its better reactive oxygen species production amplifies photodynamic therapy efficacy in female mice model. This work establishes a simple and universal approach for morphology regulation of twisted donor– $\pi$ –acceptor type photosensitizers, and also highlights the therapeutic advantages of anisotropic supramolecular self-assemblies, paving the way for next-generation phototheranostic agents.

Photodynamic therapy (PDT) has emerged as a promising oncological treatment due to its high spatiotemporal precision, noninvasiveness, minimal systemic effects and ease of operation<sup>1–3</sup>. As the pivotal core of PDT, photosensitizers generate highly toxic reactive oxygen species

(ROS) under light irradiation to cause cell death. Current organic photosensitizer design primarily focused on single molecular level, with strategies including conjugation length extension, heavy atom introduction, donor-acceptor engineering, devoted to red-shifting

<sup>1</sup>State Key Laboratory of Luminescent Materials and Devices, Guangdong Provincial Key Laboratory of Luminescence from Molecular Aggregates, School of Materials Science and Engineering, South China University of Technology, Guangzhou, China. <sup>2</sup>State Key Laboratory of Luminescent Materials and Devices & South China Advanced Institute for Soft Matter Science and Technology, South China University of Technology, Guangzhou, China. <sup>3</sup>School of Science and Engineering, Guangdong Basic Research Center of Excellence for Aggregate Science, The Chinese University of Hong Kong (CUHK-Shenzhen), Shenzhen, China. ✉e-mail: [fenggx@scut.edu.cn](mailto:fenggx@scut.edu.cn)

excitation wavelength, improving ROS generation efficiency, tuning ROS types, and so forth<sup>4–9</sup>. However, these hydrophobic photosensitizers are usually applied in the format of nanoaggregates or nanoparticles to improve their colloidal stability and biocompatibility<sup>10–12</sup>. The consequent concern is that the properties of photosensitizers at single molecular or dimer levels do not necessarily correlate with their behaviors in aggregated (e.g., enriching in tumor sites) or nanoparticle forms. Compromised fluorescence and ROS production upon loading into nanoparticles was often observed for most photosensitizers, especially for those with large planar skeletons<sup>13–15</sup>. Furthermore, these photosensitizing nanoparticles predominantly adopt isotropic spherical morphologies, exhibiting sub-optimal tumor accumulation and penetration capability<sup>16–18</sup>. Therefore, developing nano-photosensitizers with simultaneously enhanced ROS generation as well as superior tumor accumulation and penetration capabilities remains an unmet challenge.

Nanoparticle geometry plays a pivotal role in biological performance. Small spherical nanoparticles facilitate tumor accumulation due to enhanced permeability and retention (EPR) effects, but may suffer from fast tumor clearance<sup>19–21</sup>. Alternatively, anisotropic geometries such as vesicles, fibers, discs and bowls offer distinct advantages in biological applications<sup>22–25</sup>. In particular, nanorods, which mimic the bacterial morphologies, exhibit exceptional tumor targeting and penetration capabilities compared to the common nanospheres<sup>26–28</sup>. Nevertheless, achieving anisotropic rod-shaped geometry with enhanced ROS generation remains challenging. Conventional morphology shaping methods such as photolithography, film stretching, and template molding have tedious procedures and are incompatible with photophysical property modulation<sup>17</sup>. Meanwhile, polymer-/surfactant-based co-assemblies<sup>29–31</sup>, grafting strategies<sup>32,33</sup> or polymeric crystallization-driven self-assembly (CDSA)<sup>34,35</sup> function well on morphology control, but they introduce competing interactions that obscure the intrinsic molecular packing of organic photosensitizers, complicating the optimization of photophysical properties.

Supramolecular self-assembly of small molecules presents a compelling alternative to concurrently regulate their photophysical properties and biological behaviors<sup>36,37</sup>. Unlike multicomponent nanoplateforms that rely on external matrix encapsulation, supramolecular self-assemblies are driven by their intrinsic intermolecular interactions, enabling the synergistic control over molecular packing, nanostructure geometry, photophysical properties, and functional output. For instance, crystallization induces room-temperature phosphorescence or enhances ROS production, J-aggregation red-shifts absorption window<sup>38–40</sup>, while higher degree of aggregation enhances the fluorescence for molecules with aggregation-induced emission (AIE) behaviors<sup>41–43</sup>. Generally, molecules with planar  $\pi$ -conjugation cores such as porphyrins or perylene diimide (PDI) could be regulated into rod-shaped self-assemblies through introduction of flexible alkyl chains<sup>44–46</sup>, but these assemblies often suffer from non-radiative dissipation of excited energy due to the dense  $\pi$ - $\pi$  stacking, causing aggregation-caused quenching (ACQ) and reduced ROS generation<sup>13–15</sup>. In contrast, AIE photosensitizers avoid these energy losses at aggregate state, thus serving as promising candidates for developing robust nano-photosensitizers<sup>47,48</sup>. Considering the twisted molecular skeletons of AIE photosensitizers, we hypothesize that adjusting the appropriate twist-planarity balance may help achieve anisotropic rod-shaped self-assembly. However, this rod-shaped self-assembling strategy with adequate ROS generation remains uncharted.

Herein, we report a hindrance-plane-hindrance (H-P-H) molecular design skeleton to develop rod-shaped supramolecular self-assemblies, achieving simultaneously enhanced ROS generation and tumor accumulation/penetration for better PDT (Fig. 1). The strategy is elucidated with AIE photosensitizer triphenylamine-thiophene-2-(4-oxo-3-phenylthiazolidin-2-ylidene)malononitrile (TPA-S-DCR), with twisted triphenylamine (TPA) unit as electron donor (D),

thiophene as  $\pi$  bridge, and perpendicular-aligned 2-(4-oxo-3-phenylthiazolidin-2-ylidene)malononitrile (DCR) as the sterically hindered electron acceptor (A). TPA-S-DCR molecules self-assembled into rod-shaped nanoparticles under the sonication-assisted nanoprecipitation. Mechanics studies revealed that peripheral steric hindrance from TPA and DCR directs the anisotropic self-assembly of TPA-S-DCR into nanorods. The universality of the H-P-H strategy was further validated with a series of D- $\pi$ -A molecules with planar core and twisted D/A peripheries. Intriguingly, such rod-shaped self-assembly behavior was minimally influenced by polymer matrices, and the biocompatible TPA-S-DCR nanorods (TSD-Rod) with 1, 2-distearoyl-sn-glycero-3-phosphoethanolamine-poly (ethylene glycol) (DSPE-PEG) coating exhibited 1.31-fold higher ROS generation and 5.04-fold greater cancer cell uptake than spherical counterpart (TSD-Sphere). TSD-Rod also demonstrated better tumor accumulation and retention, deeper tumor penetration, thus achieving enhanced therapeutic outcome both *in vitro* and *in vivo*. This work provides a supramolecular engineering strategy for anisotropic self-assembly, which also establishes rod-shaped nano-photosensitizers as a powerful platform for next-generation phototheranostics.

## Results

### Molecular design of TPA-S-DCR

To achieve controllable rod-shaped self-assembly, a rational molecular design must balance intermolecular attraction and steric repulsion forces to direct anisotropic growth. Regulation of noncovalent interactions such as  $\pi$ - $\pi$  interactions, hydrophobic effect, hydrogen bonding are common strategies in polymeric, small molecular and their co-assembly systems<sup>49–51</sup>. Among these, steric hindrance plays a unique role in twisted small molecules, which restricts molecular rotation and confines conformational freedom, thereby guiding anisotropic growth. Interestingly, previous studies have demonstrated that steric hindrance on the  $\pi$ -bridge often disrupts ordered self-assembly<sup>52,53</sup>, a relative long and rigidified  $\pi$ -bridge often led to microscale aggregates, while long but flexible  $\pi$ -bridges disfavor anisotropic packing<sup>54,55</sup>. In this regard, we hypothesized that a H-P-H architecture, in which a planar  $\pi$ -conjugated core is flanked by sterically hindered D and/or A peripheries, would favor directional self-assembly growth of these molecules into rod-shaped structures. Such a configuration provides appropriate driving forces for unidirectional growth, and also prevents excessive aggregation that could otherwise lead to large-scale aggregates.

Based on this principle, TPA-S-DCR with twisted D- $\pi$ -A molecular geometry (featuring the H-P-H architecture) was designed for rod-shaped self-assembly exploration (Figs. S1–S4). Gaussian theoretical calculation depicted that the  $\pi$  conjugation plane extends from the benzene ring in TPA to the five-membered ring in DCR, maintaining a moderate  $\pi$ -conjugated planarity (Fig. 2a). However, the two benzene rings in TPA unit extend outside the central plane, providing the large steric hindrance at donor side. In addition, the benzene ring in DCR is perpendicularly aligned to the  $\pi$ -conjugated plane, constituting as the other steric hindrance on the acceptor side. Both TPA and DCR adopt twisted geometries that minimize planarity, weaken  $\pi$ - $\pi$  interactions from the lateral direction, and provide directional steric hindrance. Moreover, time-dependent density functional theory (TD-DFT) calculation illustrated that the highest occupied molecular orbital (HOMO) mainly distributed at TPA part and lowest unoccupied molecular orbital (LUMO) located at the thiophene and DCR segment (Fig. S26). This spatial separation of HOMO and LUMO electron clouds reduces the electron exchange energy, lowers the singlet-triplet ( $S_1$ - $T_1$ ) energy gap (0.71 eV), thereby increasing the intersystem crossing (ISC) rate and making TPA-S-DCR a potential photosensitizer.

The photophysical properties of TPA-S-DCR were subsequently evaluated. The emission of TPA-S-DCR in toluene centers at 597 nm,

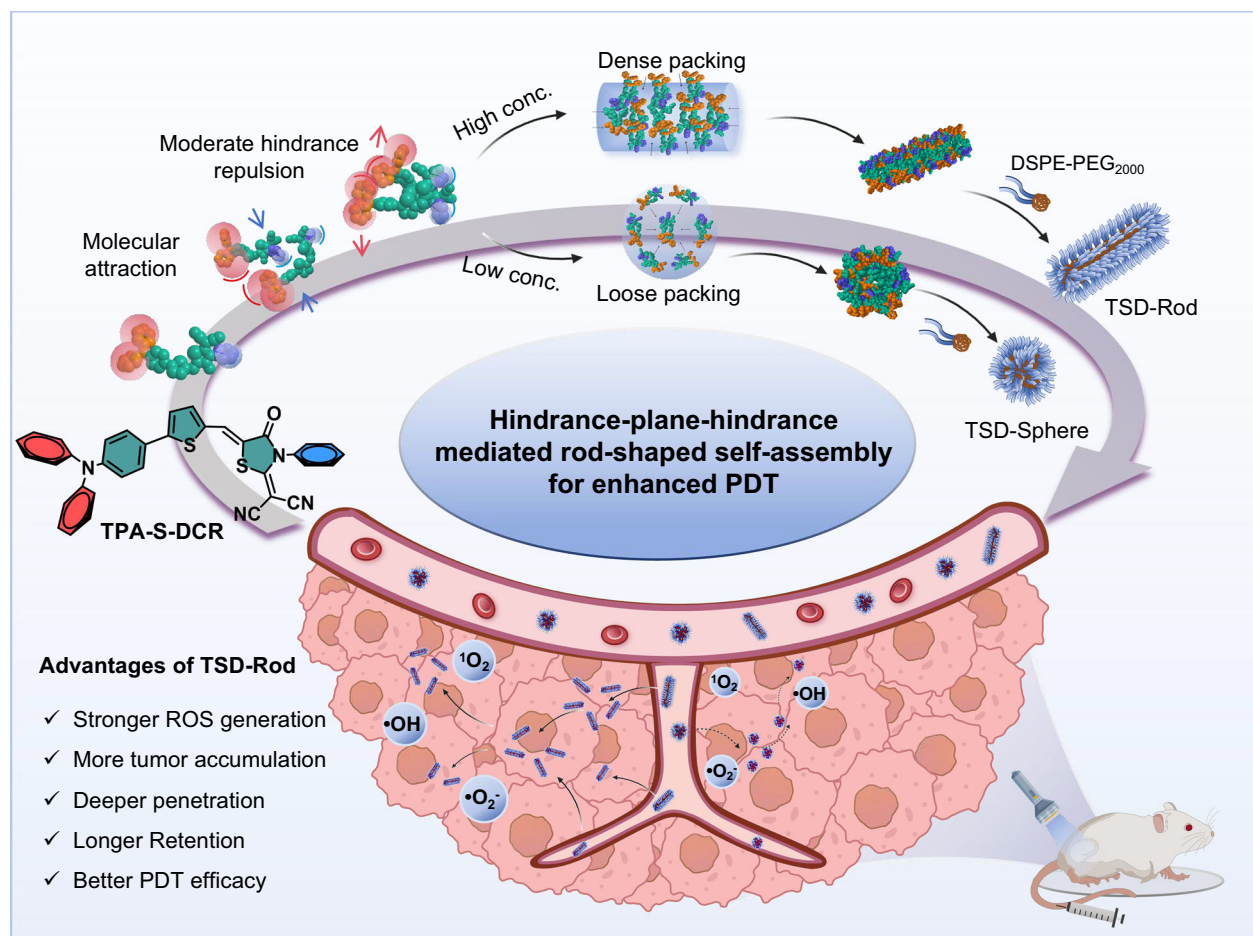


**Fig. 1 | Schematic of rod-shaped self-assembly of TPA-S-DCR and the application of TSD-Rod in PDT.** TPA-S-DCR monomers initially form dimers whereas their hindrance avoids close  $\pi$ -planar interaction. The dimers then grow into rod-shaped supramolecular self-assembly at high molecular concentrations but spherical ones at low concentrations. The obtained nanorods (TSD-Rod) and nanospheres (TSD-Sphere) are subsequently encapsulated with DSPE-PEG<sub>2000</sub> for in vivo biological applications. Compared with TSD-Sphere, TSD-Rod show stronger

reactive oxygen species (ROS) generation, higher tumor cell uptake, better tumor accumulation, deeper tumor penetration, and longer tumor retention. As a result, the obtained TSD-Rod showed better photodynamic therapy (PDT) antitumor effect. ROS include: superoxide anion free radical ( $\bullet\text{O}_2^-$ ), hydroxyl radical ( $\bullet\text{OH}$ ) and singlet oxygen ( $^1\text{O}_2$ ). Created in BioRender. Mou, X. (2025) <https://BioRender.com/6xtfrq3>.

which gradually red-shifts along with the solvent polarity increase, reaching 684 nm in dimethylsulfoxide (DMSO) (Fig. S27). In contrast, the absorption bands were less sensitive to the solvent polarity, locating from 495 nm to 518 nm. TPA-S-DCR thus exhibited a larger Stokes shift in DMSO (181 nm) over toluene (84 nm), suggesting its strong intramolecular charge transfer (ICT) effect, favoring ROS generation<sup>56,57</sup>. TPA-S-DCR also exhibited good photostability with minimal absorbance changes within 15 min of light irradiation (Fig. S28). The AIE feature of TPA-S-DCR was explored by measuring fluorescence in water/tetrahydrofuran (THF) mixture with different water fractions ( $f_w$ ) (Fig. S29a, b). TPA-S-DCR showed gradually reduced fluorescence when increasing  $f_w$  from 0 to 50%, attributing to the ICT effect. Further increasing  $f_w$  to be above 60%, TPASIC showed largely increased fluorescence, suggesting that the AIE effect of TPA-S-DCR competes over ICT effect. The fluorescence of TPA-S-DCR slightly reduced when  $f_w$  increases to 99%, hinting that a relatively high aggregation degree may hamper radiative decay and open other dissipation pathways. Therefore, the ROS generation of TPA-S-DCR was explored with varied  $f_w$ , with 2',7'-dichlorodihydrofluorescein (DCFH) as the ROS probe<sup>58</sup>. The ROS generation of TPA-S-DCR initially exhibited a similar trend as its fluorescence, showing a "V" shaped profile in the  $f_w$  ranges between 10% and 90% (Fig. S29c, d). Intriguingly, TPA-S-DCR exhibited further increased ROS generation when increasing  $f_w$

from 90% to 99%, revealing a positive correlation between aggregation degree and ROS generation ability. These results suggested that molecular packing density influences the photo-physicochemical properties of this AIE photosensitizer, thus playing an important role in regulating the performance of self-assembled nanoparticles.

### Self-assemble behavior of TPA-S-DCR

To investigate the self-assembling behavior of TPA-S-DCR, a conventional nanoprecipitation strategy without external energy input was first employed<sup>59</sup>. Specially, 1.0 mg of TPA-S-DCR was dispersed in 10 mL THF/water mixtures with varying  $f_w$ . As shown in optical images and transmission electron microscope (TEM) results (Figs. S30–S31), microneedles and even visible precipitation were observed when  $f_w$  ranges from 10 to 80%, while spherical nanoparticles were obtained at about  $f_w = 90\%$ . TPA-S-DCR failed to form rod-shaped nanoparticles under these conditions. Ultrasound-assisted nanoprecipitation was further introduced to disperse and energize TPA-S-DCR molecules for possible morphology transition<sup>60</sup>. Intriguingly, rod-shaped nanoparticles formed rapidly within only 10 s of ultrasound sonication at a  $f_w$  of 90%. With prolonged sonication time, these nanorods became longer, wider, and more uniform, reaching a morphological plateau at ~2 min (Fig. 2b, Fig. S32a). The variation of sonication amplitude (from 20 to 100%) does not affect the nanorod self-assemble behavior of

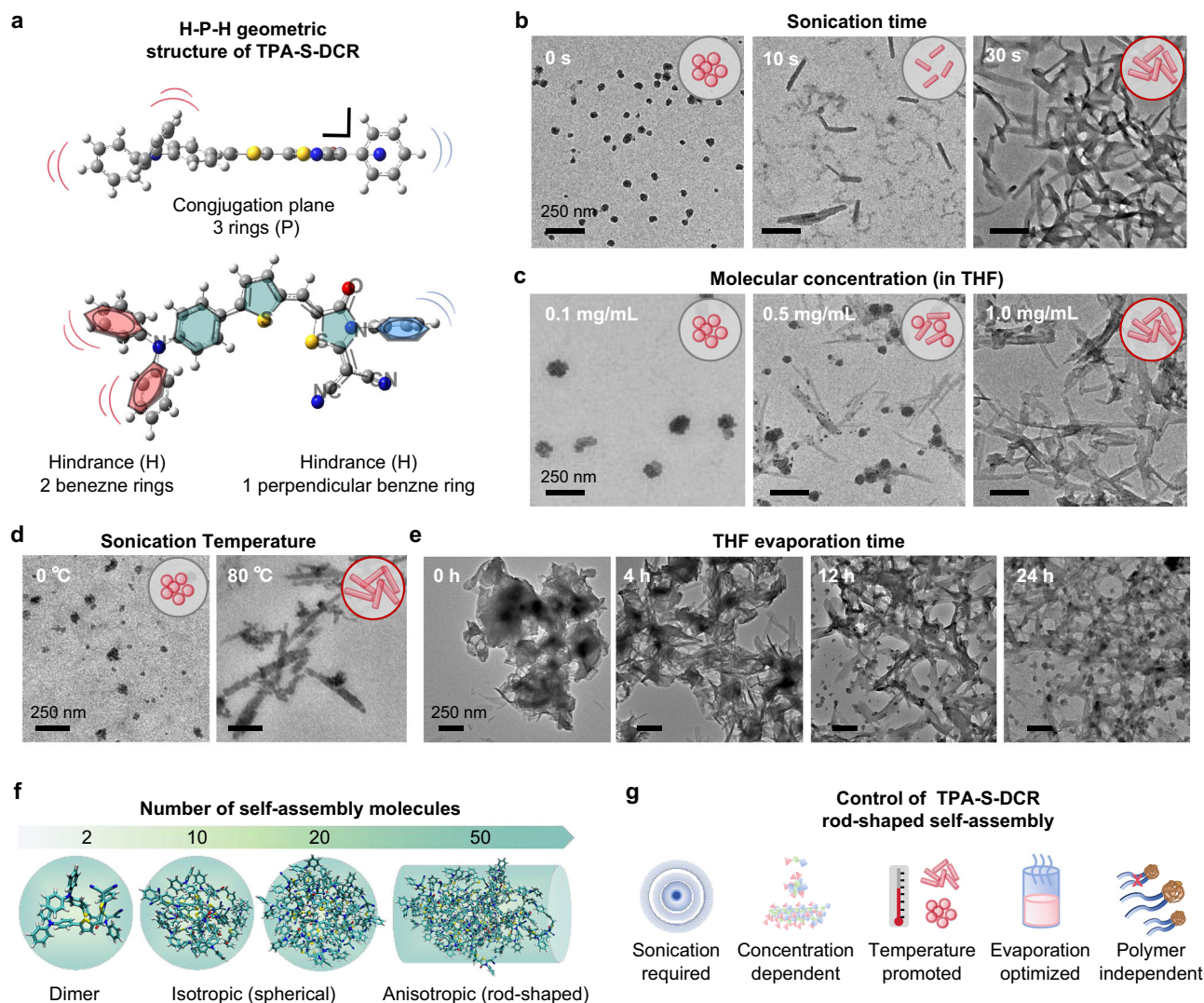


**Fig. 2 | Self-assembly of TPA-S-DCR.** **a** Optimized chemical structure of TPA-S-DCR. **b** TEM images showing the spherical to rod-shaped morphology transition with the increase of sonication time at TPA-S-DCR concentration of 1.0 mg/mL (Scale bar: 250 nm). **c** TEM images showing the self-assemble behaviors of TPA-S-DCR at different molecular concentration (under 2 min sonication) (Scale bar: 250 nm). **d** TEM images showing the self-assemble behaviors of TPA-S-DCR (1.0 mg/mL) under 0 °C and 80 °C (Scale bar: 250 nm). **e** TEM imaging showing the

morphology evolution of TPA-S-DCR self-assemblies with the evaporation of THF (Scale bar: 250 nm). **f** Molecular dynamic simulation (GROMACS) of TPA-D-DCR self-assembly with the increased molecule number increase within simulation box. **g** Schematic of influence factors towards TPA-S-DCR self-assembly. For TEM imaging,  $n = 3$  independent experiments. Created in BioRender. Mou, X. (2025) <https://BioRender.com/tf1dnvd>.

TPA-S-DCR (Fig. S32b). This rod-shaped self-assembly was also found to be strongly concentration dependent. At a low initial concentration of 0.1 mg/mL (in 1 mL THF), TPA-S-DCR only self-assembled into spherical nanoparticles, even with ultrasound sonication assistance (Fig. 2c, Fig. S33). In contrast, increasing the initial concentration to 1.0 mg/mL and above led to the gradual emergence of rod-shaped nanoparticles at the expense of spherical ones. Additionally, this rod-shaped self-assembly is an entropy-driven process, as TPA-S-DCR (at 1.0 mg/mL, with 2 min sonication) rapidly self-assembled into rod-shaped nanoparticles at 80 °C, but spherical nanoparticles at 0 °C (Fig. 2d). A high solution temperature also lowers rod-shape self-assembly threshold under sonication, where TPA-S-DCR at a low initial concentration of 0.1 mg/mL formed rod-shaped nanoparticles at 80 °C (Fig. S34). It should be noted that high solution temperature (e.g., 80 °C) alone without sonication could not induce the rod-shaped transition (Fig. S35). These results suggested that nanorod formation is an entropy-driven process, favored by ultrasound sonication and higher temperatures<sup>61,62</sup>.

The evolution of self-assembly morphology during THF volatilization was also monitored. Immediately after ultrasound sonication, the aggregates displayed poorly defined boundaries (Fig. 2e, Fig. S36). For concentrated group (the initial concentration is 1 mg/mL), partially discernible rod-shaped structures could still be distinguished. As THF gradually evaporated, the morphology shapes became more defined, with nanorods emerging from the concentrated group and nanospheres from the diluted group (0.1 mg/mL). Notably, some small spherical aggregates began to appear even in the concentrated group at a later stage (12 h to 24 h). This was likely the local Ostwald ripening<sup>63</sup>, where molecules re-dissolved from nanorods and subsequently went through re-precipitation into spherical aggregates due to low local concentration. In addition, amphiphilic block copolymers DSPE-PEG and Pluronic F127, branched polymer 8-arm polyethylene glycol-OH (PEG-OH) and dendritic polymer poly(amidoamine)-COOH (PAMAM-COOH) were further introduced to evaluate polymeric encapsulation and co-assembly effects (Fig. S37). The nanorods became thinner, shorter, and more uniform in the presence of

amphiphilic block copolymers (DSPE-PEG and F127). Instead, TPA-S-DCR assembled into nanorods with irregular outlines and rough edges in the presence of branched or dendritic polymers. This was probably due to the inherent structural rigidity and limited conformation of these branched and dendritic polymers, which hinder uniform encapsulation (compared to flexible block copolymers)<sup>64,65</sup>. The results demonstrated that although the self-assemble behavior of TPA-S-DCR was influenced by polymeric matrices to some extent, the strong intermolecular interactions between these TPA-S-DCR molecules remain the primary driving force for nanorod formation.

The stacking modes of TPA-S-DCR molecules inside nanorods were subsequently investigated. Poor powder X-ray diffraction (PXRD) crystallization signals and lack of diffuse rings under high-resolution TEM diffraction revealed the amorphous interior for both rod-shaped and spherical nanoparticles (Figs. S38–39). Moreover, both nanoparticles showed similar absorption peaks (~500 nm) as their monomers in THF (495 nm), suggesting the absence of ordered H- or J-type aggregation (Fig. S40). Quantification of packing density showed that nanorods had a higher TPA-S-DCR density of 39.67 nm<sup>-3</sup>, which was about ~3-fold of nanospheres (13.10 nm<sup>-3</sup>) (Table S1). The result indicated that rod-shaped self-assembly possesses tighter molecular

packing, which was likely to enhance the internal restriction of intramolecular motions, thus favoring AIE effect and ROS generation. In addition, molecular dynamic simulations using GROMACS were further conducted in an 8 × 8 × 8 nm<sup>3</sup> simulation box. As molecule number increases, TPA-S-DCR exhibited anisotropic growth tendency, potentially leading to rod-shaped aggregation (Fig. 2f). This simulation result was consistent with the concentration-dependent morphology transition. Additionally, four typical dimer conformations were extracted from the simulation box, which depicted disordered stacking modes, stabilized by repulsion of these peripheral hindrance groups (Fig. S41). No obvious  $\pi$ - $\pi$  interactions or specific atom-atom interactions were determined in these dimers since most interatomic distances exceeded 4 Å. In summary, we demonstrated a unique rod-shaped self-assembly process for TPA-S-DCR, which was concentration-, temperature-, and sonication-dependent (Fig. 2g).

### H-P-H-regulated rod-shaped self-assembly

The fundamental structure determinant for the anisotropic growth into rod-shaped nanostructures was further evaluated with a series of H-P-H structured molecules (Fig. 3a, Fig. S1–S25). Within TPA-S-DCR (2), TPA contributes higher steric hindrance (two out-of-plane benzene

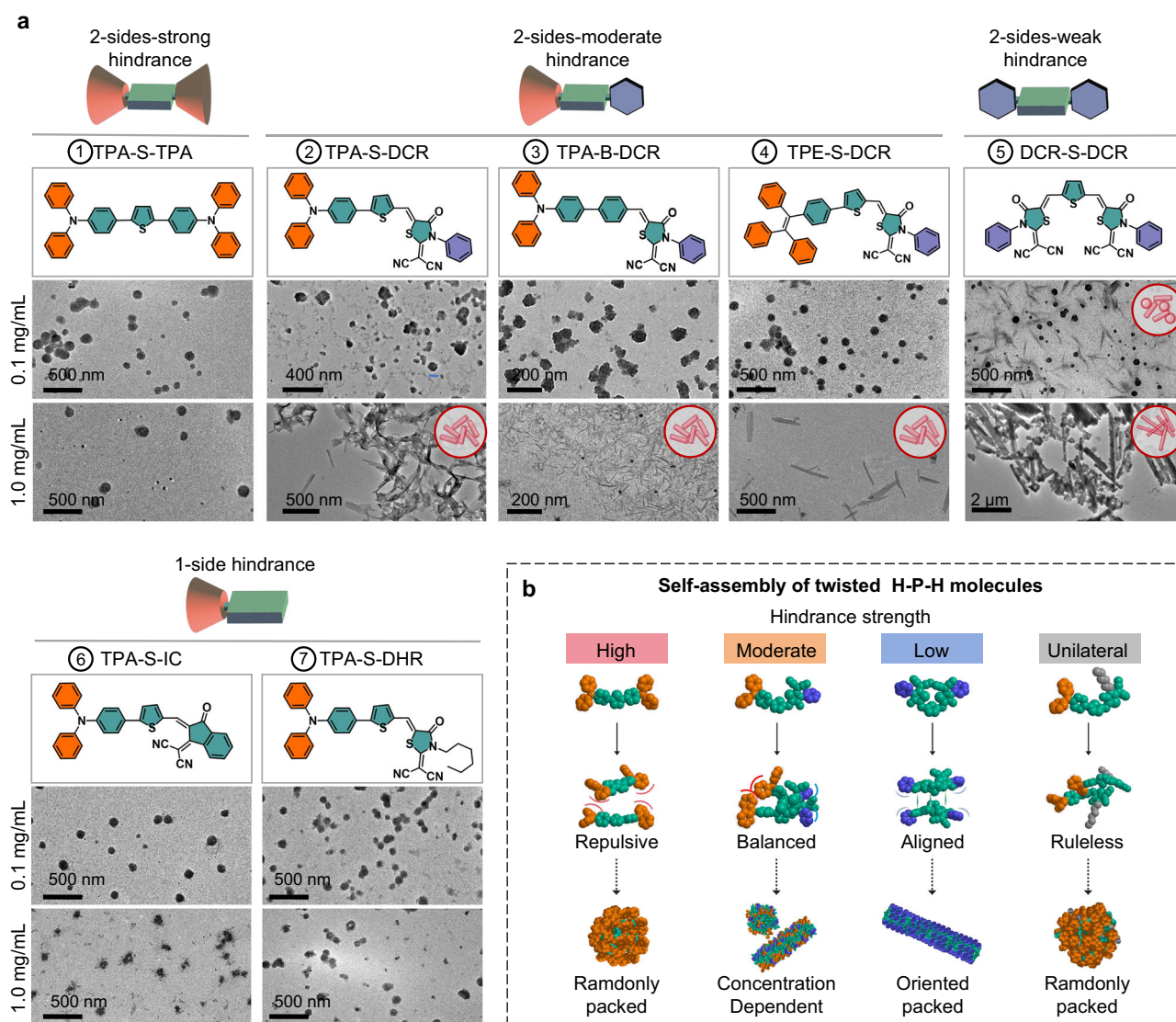


**Fig. 3 | Supramolecular self-assembly based on H-P-H designing template.**

**a** Self-assembled morphologies of molecules with distinct hindrance effects (with the assistance of 2 min sonication) ( $n = 3$  independent experiments). **b** Schematic of

the influence of structural hindrance strength on supramolecular self-assembly towards morphology control. Created in BioRender. Mou, X. (2025) <https://BioRender.com/tf1dnvd>.

rings) but shorter planar conjugation, while DCR contributes longer planar conjugation with less steric bulk (one perpendicular benzene ring). Their combination resulted in a successful, concentration-dependent rod-shaped self-assembly. To verify the generality of the H-P-H principle, two similar derivatives were synthesized: TPA-B-DCR (3) in which the thiophene  $\pi$  bridge was replaced by a benzene (B) ring (a minor change in conjugation and steric profile); TPE-S-DCR (4) in which TPA was substituted by tetraphenylvinyl (TPE) group with a higher steric hindrance while maintaining similar planar conjugated plane. Both TPA-B-DCR and TPE-S-DCR self-assembled into spherical nanoparticles at low initial concentration (0.1 mg/mL), but nanorods at higher concentration (1.0 mg/mL) under 2 min sonication. Their similar self-assembly behavior to TPA-S-DCR expands the scope of H-P-H strategy for concentration-dependence rod-shaped self-assembly.

Additionally, a highly hindered symmetric molecule TPA-S-TPA (1) with two strong distorted peripheries was also examined. TPA-S-TPA only formed spherical aggregates regardless of concentration, temperature and ultrasound sonication. This should be caused by its high proportion of hindrance groups (two out-of-plane benzene rings) on both TPA sides, which provide high degree of repulsion and disrupt the long-range oriented stacking, thus hindering rod-shaped self-assembly. In contrast, another symmetric molecule DCR-S-DCR (5), with lower steric hindrance at both peripheries, rapidly self-assembled into micro-scale rod-shaped aggregates even at low initial concentrations. This should be caused by the extended central planar conjugation of DCR, which enhances planar  $\pi$ - $\pi$  interactions and counterbalances the steric hindrance, leading to rapid micro-scaled rod-like self-assembly with less controllability.

To further probe the roles of terminal steric hindrance, TPA-S-IC (6) and TPA-S-DHR (7), with reduced steric hindrance at acceptor periphery were synthesized. In TPA-S-IC, the perpendicular benzene ring was replaced by a fused conjugated ring that extends  $\pi$ -conjugated plane. While in TPA-S-DCR, the perpendicular benzene ring was replaced by a flexible hexyl chain, which largely reduced peripheral steric hindrance. Both molecules self-assembled into spherical nanoparticles under all conditions, suggesting that crucial roles of terminal  $\pi$ -conjugated steric hindrance in controlling molecular alignment and promoting the anisotropic rod-shaped self-assembly. When the steric hindrance on both peripheries was minimized by changing TPA to *N,N*-dimethylaniline, the exemplified molecule MeA-S-MeA (8) self-assembled into the mixture of spherical and rod-shaped nanoparticles, regardless of concentrations (Fig. S42). The molecular conformation of MeA-S-MeA completely deviated from the H-P-H rule, thus the directional growth becomes stochastic and the self-assembly morphologies are less predictable and controllable.

Therefore, the H-P-H architecture represents a rational and effective design strategy to achieve rod-shaped self-assemblies (Fig. 3b). Molecules with excessive steric hindrance on both peripheries (e.g., TPA-S-TPA) are prone to spherical aggregation due to overwhelming intermolecular repulsion. Those with balanced steric hindrance and planar conjugation (e.g., TPA-S-DCR, TPA-B-DCR, and TPE-S-DCR) can form rod-shaped nanoparticles in a concentration-dependent manner, where denser stacking at high concentrations enhances steric restriction and repulsion, favoring anisotropic growth. Molecules with reduced hindrance rely increasingly on planar interactions; for instance, DCR-S-DCR exhibits rapid micro-rod formation. When hindrance on one side is removed (e.g., TPA-S-IC and TPA-S-DHR), the suppression of molecular slippage is lost, and isotropic spherical assembly dominates.

### Characterization of TPA-S-DCR nanorods (TSD-Rod)

To improve colloidal stability and biocompatibility, amphiphilic polymer DSPE-PEG was introduced to co-assemble with TPA-S-DCR under different initial concentrations to form colloidal stable nanoparticles

(termed as TSD-Rod and TSD-Sphere) (Fig. 4a). TEM images showed uniformly distributed TSD-Rod and TSD-Sphere with well-defined and smooth particle edges (Fig. 4b). Atomic force microscopy (AFM) analysis further supported the distinct rod-shaped and spherical nanostructures (Fig. 4c, Fig. S43). Geometric parameters and packing densities were subsequently quantified (Fig. 4d, Table S1), TSD-Rod exhibited a typical length of ~200 nm and an average diameter of ~20 nm, while TSD-Sphere had diameters of ~60 nm. The overall morphological features of these nanoparticles were further statistically characterized by static light scattering (SLS) and dynamic light scattering (DLS) (Fig. 4d). The radius of gyration ( $R_g$ ) and hydrodynamic radius ( $R_h$ ) were determined to be 47.11 nm and 8.26 nm for TSD-Rod, and 33.64 nm and 32.87 nm for TSD-Sphere, respectively. A high  $R_g/R_h$  ratio (5.7) of TSD-Rod suggested their anisotropic geometry, whereas the nearly unity  $R_g/R_h$  ratio (1.02) of TSD-Sphere confirmed their isotropic spherical nature, consistent to the microscopic observations. Additionally, the translational diffusion coefficient ( $D_t$ ) and rotational diffusion coefficient ( $D_r$ ) for TSD-Rod were determined to be  $2.96 \times 10^7$  nm<sup>2</sup>/s and  $9877.89$  s<sup>-1</sup>, which were about ~4.0- and ~1.9-fold higher than those of TSD-Sphere ( $D_t = 7.43 \times 10^6$  nm<sup>2</sup>/s,  $D_r = 5157.57$  s<sup>-1</sup>), hinting the better movement and mucosal penetration ability of TSD-Rod<sup>66-68</sup>. Further light scattering analysis suggested similar zeta potentials for TSD-Rod (-29.2 mV) and TSD-Sphere (-31.0 mV) in water (Fig. S44), due to the presence of PEG shell. Both TSD-Rod and TSD-Sphere also showed minimally changed sizes, morphologies and surface potentials upon 15 days' storage under physiological conditions, indicating their excellent colloidal stability (Figs. S44-S46).

Both nanoparticles showed similar absorption and emission spectra. The lower fluorescence intensity of TSD-Rod (~55.5% of TSD-Sphere) hinted its excited state energy was dissipating through other pathways (Fig. 4e). Thus, the photo-induced ROS generation was evaluated. Using DCFH as the total ROS probe, TSD-Rod exhibited ~1.31-fold higher ROS generation ability than TSD-Sphere as manifested by DCF fluorescence enhancement factors (241.7 versus 184.5) (Fig. 4f, Fig. S47a-d). Additionally, dihydrorhodamine 123 (DHR123), hydroxyphenyl fluorescein (HPF), and 9',10'-anthracenediyl-bis(methylene)-dimalonic acid (ABDA) were further used to detect the generation of superoxide anion radical ( $\bullet\text{O}_2^-$ ), hydroxyl radical ( $\bullet\text{OH}$ ) and singlet oxygen ( $^1\text{O}_2$ ), respectively. TSD-Rod induced ~1.27-fold higher fluorescence enhancement of DHR123 as compared to TSD-Sphere (44.53 versus 34.97), suggesting a more efficient  $\bullet\text{O}_2^-$  generation (Fig. 4g, Fig. S47e-h). The HPF assay also suggested a faster fluorescence ascending profile for TSD-Rod, with  $\bullet\text{OH}$  generation reaching 1.69-fold of TSD-Sphere (58.99 versus 34.85) after 4 min light irradiation (Fig. 4h, Fig. S47i-l). ABDA degradation also showed a better  $^1\text{O}_2$  generation ability of TSD-Rod, showing a 1.39-fold higher absorbance decline rate than TSD-Sphere (Fig. 4i, Fig. S48). These results clearly demonstrated that the TSD-Rod exhibited enhanced ROS generation compared to TSD-Sphere. Notably, the difference was largely attributed to the assembling difference rather than polymer encapsulation, as pure TPA-S-DCR nanorods without DSPE-PEG also exhibited ~1.33-fold higher total ROS generation over TPA-S-DCR nanospheres (Fig. S49). Moreover, both TSD-Rod and TSD-Sphere exhibited slightly increased ROS generation over their bare counterparts, as DSPE-PEG confines the molecular packing and reduces nanoparticle sizes during the assemble process (Fig. S50). However, post-encapsulation reduced the ROS generation for both nanorods and nanospheres as it doesn't affect molecular packing of TPA-S-DCR but reduces the interaction with surrounding oxygen (Fig. S51). Finally, stability tests suggested that both TSD-Rod and TSD-Sphere also demonstrated consistent fluorescence and ROS generation ability at different physiological conditions (Figs. S52-S54).

The underlying mechanism could be explained from the titration experiments mentioned above (Fig. S29), where increasing  $f_w$  from 90 to 99% led to decreased fluorescence but increased ROS

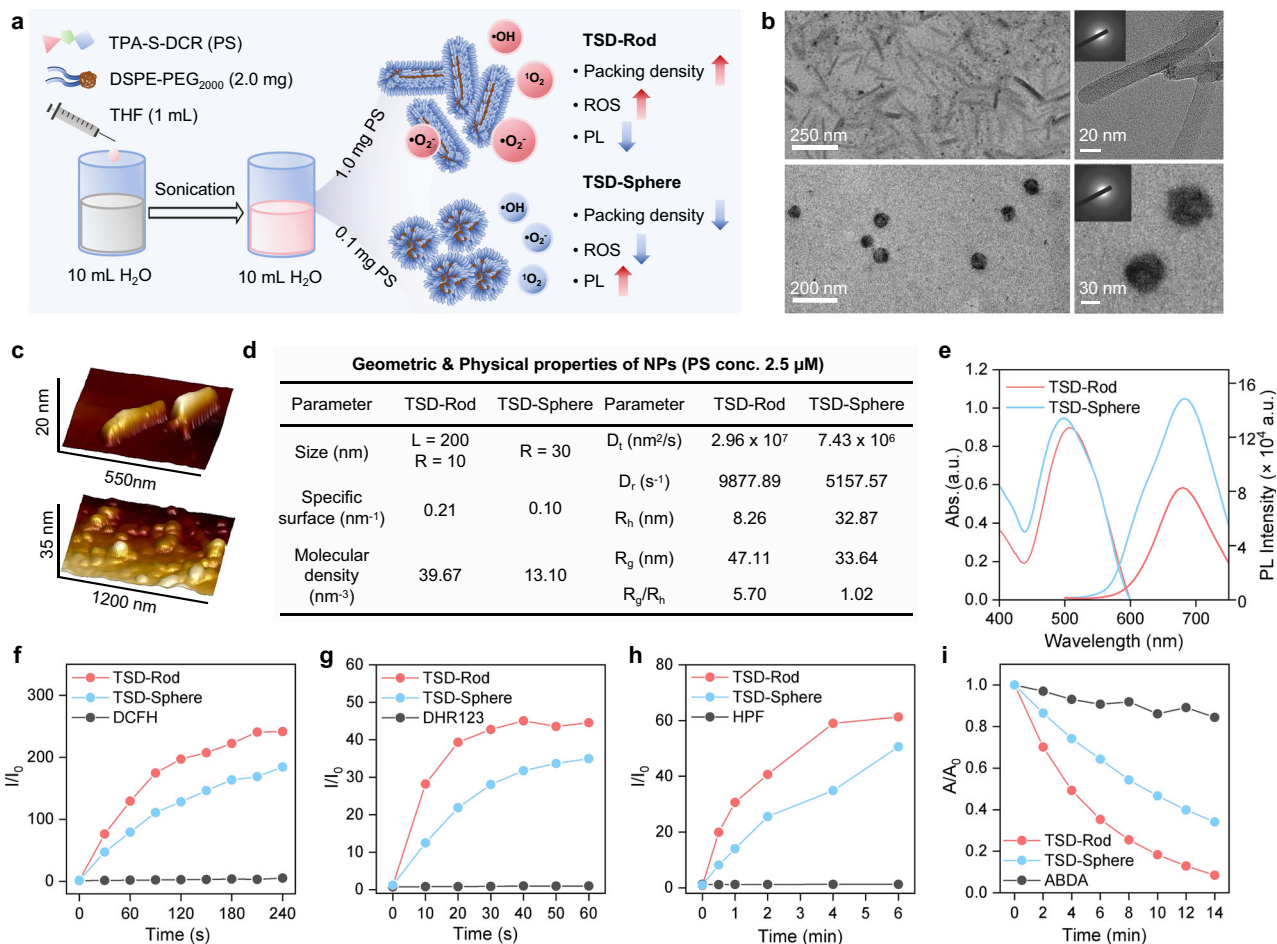


**Fig. 4 | Characterization of TSD-Rod and TSD-Sphere.** **a** Schematic of the preparation of TSD-Rod/TSD-Sphere and the summary of their properties. PS refers to photosensitizer, ROS refers to reactive oxygen species, PL refers to photoluminescence. Created in BioRender. Mou, X. (2025) <https://BioRender.com/tfldnvd>. **b** TEM images and diffraction patterns of TSD-Rod/TSD-Sphere ( $n = 3$  independent experiments). **c** 3D AFM images of TSD-Rod/TSD-Sphere. **d** Table showing the geometric and physical properties of TSD-Rod and TSD-Sphere. **e** Absorption and PL spectra of TSD-Rod/TSD-Sphere. TPA-S-DCR concentration is 80  $\mu\text{M}$ . a.u. refers to arbitrary unit. **f** Total ROS generation detected by DCFH probe,

which was reflected by DCF fluorescence enhancement. **g**  $\text{O}_2^-$  generation detected by DHR123 probe. **h**  $\text{OH}$  generation detected by HPF probe.  $I_0$  and  $I$  refer to fluorescence intensity of specific ROS probe before and after light irradiation (i)  $\text{O}_2$  generation detected by ABDA probe, which was reflected by the decrease of ABDA absorbance ( $A/A_0$ , where  $A_0$  and  $A$  refer to the absorbance of ABDA before and after light irradiation). White light irradiation: 20  $\text{mW}/\text{cm}^2$ ; TPA-S-DCR concentration is 10  $\mu\text{M}$ . Two-tailed Student's  $t$  test was performed for comparisons between two groups. Source data are provided in Source Data file.

generation. This trend suggested that denser molecular packing (at high  $f_w$ ) possibly promoted ISC process, favoring ROS generation over fluorescence emission. Dynamic tracking of pure TPA-S-DCR self-assembly at different concentrations (0.1, 0.3, 0.5 to 1.0  $\text{mg}/\text{mL}$ ) also supported this hypothesis: higher concentration led to decreased photoluminescence (Fig. S40) with synchronously preferential formation of rod-shaped nanostructures. Besides, geometric analysis also suggested a larger specific surface area of TSD-Rod (0.21  $\text{nm}^{-1}$ ) compared to TSD-Sphere (0.10  $\text{nm}^{-1}$ ), implying that a greater interface for oxygen interaction, which also contributed to the enhanced ROS generation. In addition, similar phenomena were also found for TPA-B-DCR and TPE-S-DCR with H-P-H architectures: their rod-shaped supramolecular self-assemblies generated more ROS but emitted weaker fluorescence than the corresponding nanospheres (Fig. S55–S56). In contrast, for photosensitizers lacking rod-shaped self-assembly tendency (e.g., TPA-S-DHR), they self-assembled into nanospheres at both low and high initial concentrations, and these nanospheres exhibited similar fluorescence and ROS generation capabilities (Fig. S57). These results further validated that appropriate H-P-H molecular design enabled rod-shaped self-assembly with enhanced ROS generation.

### In vitro PDT with TSD-Rod

The cellular uptake behaviors of TSD-Rod and TSD-Sphere were evaluated in both cancerous and normal cell lines, with murine-derived 4T1 cell line, NCTC clone 929 (L929) cell line as the model cell lines. Confocal laser scanning microscope (CLSM) images suggested that cellular internalization of nanoparticles reached the maximum with 5 h incubation (Fig. S58–S59). TSD-Rod outperformed TSD-Sphere in internalizing into the 4T1 cancer cells by 2.77-fold in terms of fluorescence brightness, while smaller difference was observed in L929 normal cells (Fig. 5a, b). Considering the lower average fluorescence per nanoparticle, TSD-Rod exhibited a total 5.04-fold higher uptake in 4T1 cells than TSD-Sphere. The flow cytometry results also corroborated these findings, confirming the selectively passive targeting of TSD-Rod towards cancer cells (Fig. 5c). Furthermore, enhanced internalization in human-derived MCF-7 cancer cells was also observed for TSD-Rod (1.29-fold increase over TSD-Sphere), further confirming the cancer-preferable uptake of TSD-Rod (Fig. S60). This internalization difference was likely attributed to the anisotropic rod shape and the distinct endocytic behaviors of cancer cells, which included micropinocytosis that facilitates the engulfment of larger or elongated nanostructures<sup>69</sup>. In contrast, normal cells rely mainly on the common clathrin-mediated

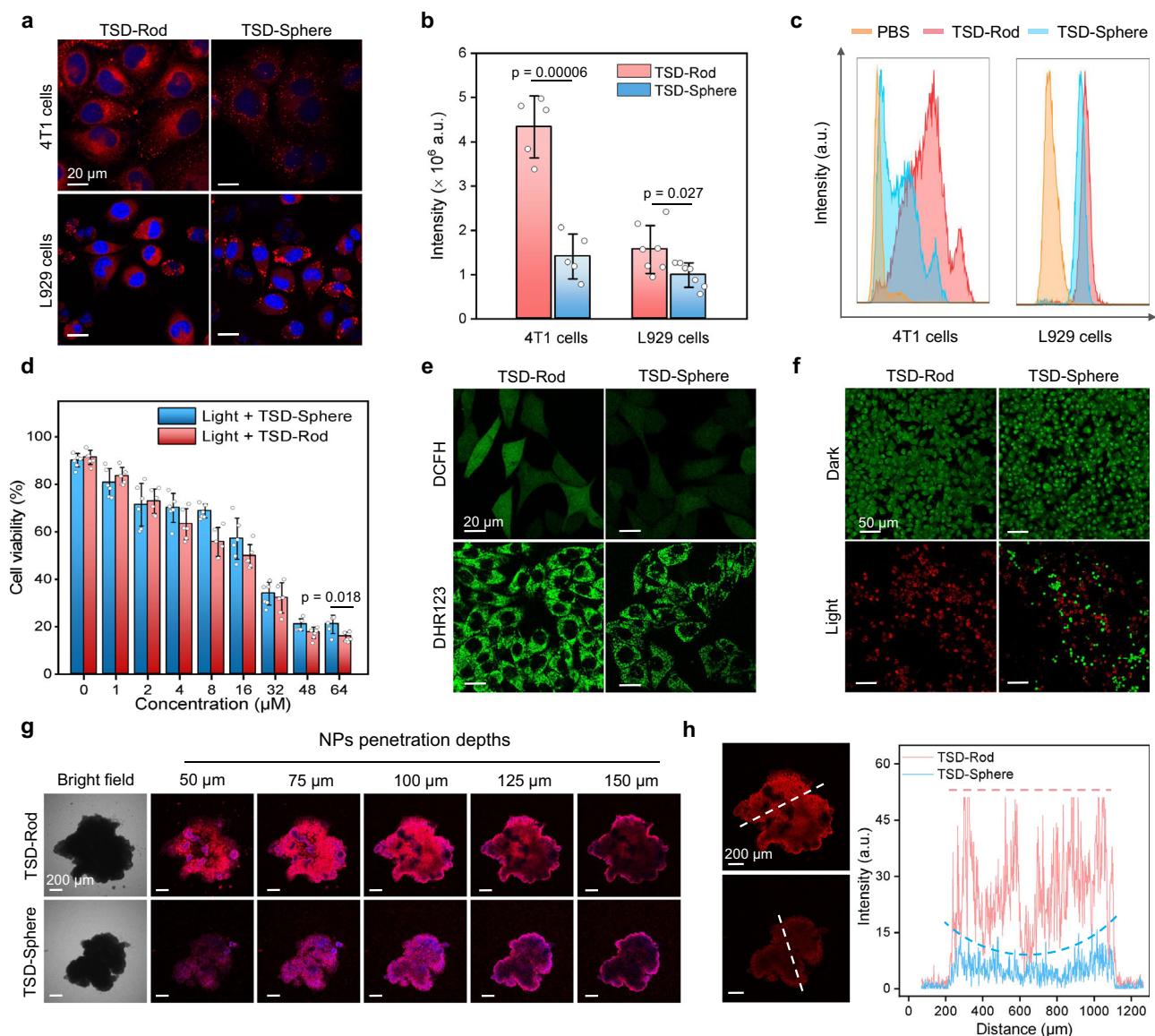


**Fig. 5 | In vitro PDT evaluation of TSD-Rod and TSD-Sphere.** **a** CLSM images showing the cellular uptake of TSD-Rod and TSD-Sphere in cell 4T1 and cell L929 at 5 h (Scale bar: 20  $\mu\text{m}$ ). **b** Histogram statistics of TSD-Rod/TSD-Sphere uptake in (a). Data are presented as mean  $\pm$  standard deviation (SD) ( $n = 5$  independent samples for 4T1 cells,  $n = 7$  independent samples for L929 cells). **c** Flow cytometry analysis of cellular uptake of TSD-Rod/TSD-Sphere in both cells line. **d** Viabilities of 4T1 cells after TSD-Rod/TSD-Sphere incubation and light irradiation (40  $\text{mW}/\text{cm}^2$ , 20 min). Data are presented as mean  $\pm$  SD ( $n = 6$  independent samples). **e** CLSM images showing intracellular ROS generation with DCFH and DHR123 (20  $\mu\text{M}$ ) as ROS probes (Scale bar: 20  $\mu\text{m}$ ). **f** CLSM images showing live/dead of 4T1 cells after TSD-

Rod/TSD-Sphere incubation and light irradiation, accessed by calcein AM/PI assay (Scale bar: 50  $\mu\text{m}$ ). **g** CLSM images of 3D tumor spheroids at different depths, after incubation with TSD-Rod/TSD-Sphere (Scale bar: 200  $\mu\text{m}$ ). **h** Cross-section fluorescence profile of TSD-Rod/TSD-Sphere at a depth of 100  $\mu\text{m}$  in the 3D tumor spheroids, showing their centripetal diffusion behaviors (Scale bar: 200  $\mu\text{m}$ ). For CLSM imaging,  $n = 3$  independent experiments. a.u. refers to arbitrary unit. Two-tailed Student's  $t$  test was performed for comparisons between two groups. A significance level of  $p < 0.05$  was utilized for determining statistical significance. Source data are provided in Source Data file.

endocytosis and caveolae-mediated endocytosis<sup>26,60,70,71</sup>, leading to a comparable uptake of nanorods and nanospheres in normal cells.

Cell viability was tested through methyl thiazolyl tetrazolium (MTT) assay. Without light exposure, both TSD-Rod and TSD-Sphere showed negligible cytotoxicity, proving their excellent biocompatibility (Fig. S61). Under white light irradiation (40  $\text{mW}/\text{cm}^2$  for 20 min), TSD-Rod exhibited much stronger killing effect over TSD-Sphere under all tested concentrations, with the half-maximum inhibitory concentrations ( $\text{IC}_{50}$ ) of 8  $\mu\text{M}$  and 32  $\mu\text{M}$  for TSD-Rod and TSD-Sphere, respectively (Fig. 5d). In addition, increasing light power to 100  $\text{mW}/\text{cm}^2$  greatly promoted ROS generation and enhanced photodynamically killing effect of both TSD-Rod and TSD-Sphere (Fig. S61). The intracellular ROS generation ability was then assessed in 4T1 cells,

using DCFH-DA and DHR123 for total ROS and  $\bullet\text{O}_2$  detection. After 5 h incubation followed by 10 min of white light irradiation (20  $\text{mW}/\text{cm}^2$ ), CLSM images showed bright green fluorescence in both groups, with TSD-Rod-treated cells exhibiting 3.07-fold (DCFH) and 1.43-fold (DHR123) higher intensities, indicative of more efficient intracellular ROS generation (Fig. 5e, Fig. S62). The notably larger difference at intracellular ROS level compared to the in vitro solution tests should be attributed to the higher cellular uptake of TSD-Rod. Additionally, live/dead cell staining experiment with calcein acetoxyethyl ester (AM) and propidium iodide (PI) assay further revealed the extensive cell death in TSD-Rod-treated 4T1 cells post-irradiation, whereas only partial cell death was observed in TSD-Sphere-treated group (Fig. 5f). Cell apoptosis and necrosis were quantitatively assessed by flow

cytometry with Annexin V-APC and 4',6-diamidino-2-phenylindole (DAPI) as the indicators (Fig. S63). Upon light irradiation, 32.80% of cells treated with TSD-Rod underwent late apoptosis, increased by ~3-fold compared to TSD-Sphere (10.29%). The early apoptosis rate was also higher for TSD-Rod (64.42%) than TSD-Sphere (49.05%) post-irradiation, underscoring the superior photodynamic ablation capacity of the rod-shaped nanoparticles.

Given the much larger  $D_t$  and  $D_r$  coefficients, TSD-Rod is expected to penetrate deeper into tumor tissues. This hypothesis was tested using a 3D tumor spheroids model. 4T1 tumor spheroids (diameter of ~1 mm) were incubated with TSD-Rod or TSD-Sphere for 8 h, and the nucleus were stained with Hoechst33342. Sectional images of tumor spheroids from CLSM tomography scan were collected at different depths (0–250  $\mu\text{m}$ ). Brighter fluorescence of TSD-Rod was observed cross all the depths, suggesting its higher penetration into tumor spheroids than TSD-Sphere (Fig. 5g, Fig. S64a). At the depth of 75–100  $\mu\text{m}$ , the sectional total intensity reached the highest, where TSD-Rod exhibited 4.60-fold higher than TSD-Sphere (Fig. S64b). The better penetration effect was also reflected by the centripetal diffusion, where the fluorescence of TSD-Rod spread into the spheroid core (e.g., at a depth of 100  $\mu\text{m}$ ), while TSD-Sphere remained largely confined to the spheroid periphery (Fig. 5h). After light irradiation, the tumor spheroids were stained with PI to reveal cell death at different depths. Extensive red fluorescence throughout the spheroid volume in TSD-Rod-treated group was observed, highlighting effective phototoxicity in deeper tumor regions (Fig. S65). In contrast, TSD-Sphere delivered minimal damage to these cells deeper seated inside tumor spheroid. The better tumor penetration and photodynamic killing ability of the TSD-Rod was thus preliminarily proved.

### Biodistribution and tumor accumulation of TSD-Rod

The *in vivo* biodistribution, tumor enrichment and penetration of both TSD-Rod and TSD-Sphere were further investigated on tumor-bearing balb/c female mice. 4T1 cells were inoculated into the upper part of the right leg of 6-week-old balb/c mice to construct subcutaneous tumor-bearing murine model. 100  $\mu\text{L}$  of isotonic nanoparticle dispersion (TPA-S-DCR conc. 750  $\mu\text{g}/\text{mL}$ ) were injected through the tail vein. Fluorescence imaging suggested that tumor-site signal started to emerge at 4 h post-injection, gradually increased, and reached the plateaus at 12 h for TSD-Rod and 8 h for TSD-Sphere, respectively (Fig. 6a, b, Fig. S66). After correcting for inherent brightness differences between the nanoparticles, TSD-Rod achieved 1.67-fold higher tumor enrichment than TSD-Sphere. Tumor fluorescence signal gradually declined thereafter, due to the nanoparticle metabolism and body clearance. *Ex vivo* imaging of organs collected at 12 h post injection also suggested a 1.44-fold higher tumor accumulation of TSD-Rod over TSD-Sphere (Fig. 6, d, Fig. S67), in consistent with *in vivo* imaging results.

To further evaluate their tumor penetration ability, tumor tissues collected at 8 h post injection (as TSD-Rod and TSD-Sphere exhibited similar *ex vivo* tumor accumulation ability at this time point, Fig. S67–S68) were sectioned at varying depths (i.e., surface, one quarter, one half, and three quarter), followed by CLSM scanning (Fig. 6e). While both TSD-Rod and TSD-Sphere were detectable throughout the tumor mass, TSD-Rod displayed more uniform distribution and stronger fluorescence across all slices, indicating superior tumor penetration. Unlike the *in vitro* tumor spheroids model, the *in vivo* tumor microenvironment allowed dynamic nanoparticle redistribution, including penetration, extraction, and clearance into blood vessels. Thus, the more uniform distribution across all depths of TSD-Rod was not only caused by their deeper penetration ability, but also contributed by their prolonged retention. These attributes collectively suggested the potential of TSD-Rod towards enhanced tumor accumulation, penetration and retention.

### *In vivo* PDT of TSD-Rod

The *in vivo* PDT experiments were subsequently carried out (Fig. 7a). The mice were randomly divided into 6 groups: phosphate buffered saline (PBS), PBS + Light (L), TSD-Rod, TSD-Rod + L, TSD-Sphere and TSD-Sphere + L. Upon tumor volumes reached ~90  $\text{mm}^3$  on day 0, 200  $\mu\text{L}$  of PBS or isotonic nanoparticle dispersion (TPA-S-DCR conc. 750  $\mu\text{g}/\text{mL}$ ) was intravenously injected through the tail. Mice in light treatment groups were exposed to white light irradiation (100  $\text{mW}/\text{cm}^2$ ) for 30 min at 8 h post-injection. The treatment was repeated on day 5. Body weights and tumor volumes were consecutively monitored over 14 days (Fig. 7b, Fig. S69). Compared to the PBS + L control group in which tumor volume increased to ~589.0  $\text{mm}^3$ , both TSD-Rod + L and TSD-Sphere + L groups showed obvious tumor growth suppression. TSD-Rod + L group showed remarkably inhibited tumor growth (~67.8  $\text{mm}^3$ ) after first PDT treatment. While TSD-Sphere + L group only exhibited slight tumor inhibition (~235.8  $\text{mm}^3$ ) even after the second PDT treatment. On day 14, the mice were sacrificed, and the tumors were extracted and weighed (Fig. 7c, Fig. S70). Tumors from TSD-Rod + L group weighted ~50.3 mg, less than those from TSD-Sphere + L (~173.9 mg) and PBS + L (~469.2 mg) groups. Visual examination of tumors also confirmed enhanced tumor ability by the PDT of TSD-Rod (Fig. S71).

Histological and immunofluorescence analyses were conducted to further assess therapeutic outcomes (Fig. 7d). Hematoxylin and eosin (H&E) staining showed extensive cellular necrosis in the tumor from TSD-Rod + L group while tumors from TSD-Sphere + L and PBS + L groups remained largely intact. Likewise, Terminal deoxynucleotidyl transferase dUTP nick end labeling (TUNEL) staining revealed a higher proportion of apoptotic DNA fragmentation in the TSD-Rod + L group. Ki67 immunostaining showed largely reduced green fluorescence, indicative of reduced tumor cell proliferation ability following TSD-Rod-based PDT and further supporting the effective tumor cell ablation by TSD-Rod-mediated PDT.

The *in vivo* biosafety and biocompatibility of nanoparticles were also evaluated on healthy mice after intravenous administration. H&E staining of heart, liver, spleen, lung and kidney showed minimal histological abnormalities and difference between TSD-Rod, TSD-Sphere and the control groups (Fig. 7e). Blood routine and biochemistry tests were also conducted, where the red blood cells, white blood cells, platelets, liver function and renal function indicators of mice turned out to be within the normal range (Fig. 7f, Fig. S72–S73). These results confirm the favorable biocompatibility and systemic safety of TSD-Rod.

### Discussion

In conclusion, we herein report a H-P-H molecular design strategy for constructing twisted D- $\pi$ -A type photosensitizers capable of self-assembling into rod-shaped nanostructures, enabling morphology-regulated phototheranostic performance. In the aspect of self-assembly, we achieved controllable morphology regulation of these twisted photosensitizers into nanospheres and nanorods (e.g., TPA-S-DCR, TPA-B-DCR and TPE-S-DCR) by fine-adjusting the  $\pi$ -conjugated steric hindrances at D/A peripheries. As for photophysical property changes, the denser packing inside nanorods modulated the excited-state energy dissipation pathways—promoting intersystem crossing—thereby enhancing ROS generation. Specifically, TSD-Rod exhibited higher aqueous (1.31-fold) and intracellular (3.07-fold) ROS generation than TSD-Sphere counterparts. TSD-Rod also showed better biological performance: it exhibited higher tumor cell uptake (5.04-fold), deeper penetration in *ex vivo* 3D spheroid and *in vivo* tumor tissues, higher tumor enrichment, and longer tumor retention over TSD-Sphere. The enhanced ROS generation and tumor enrichment/penetration/retention cooperatively enhanced the photodynamic therapeutic

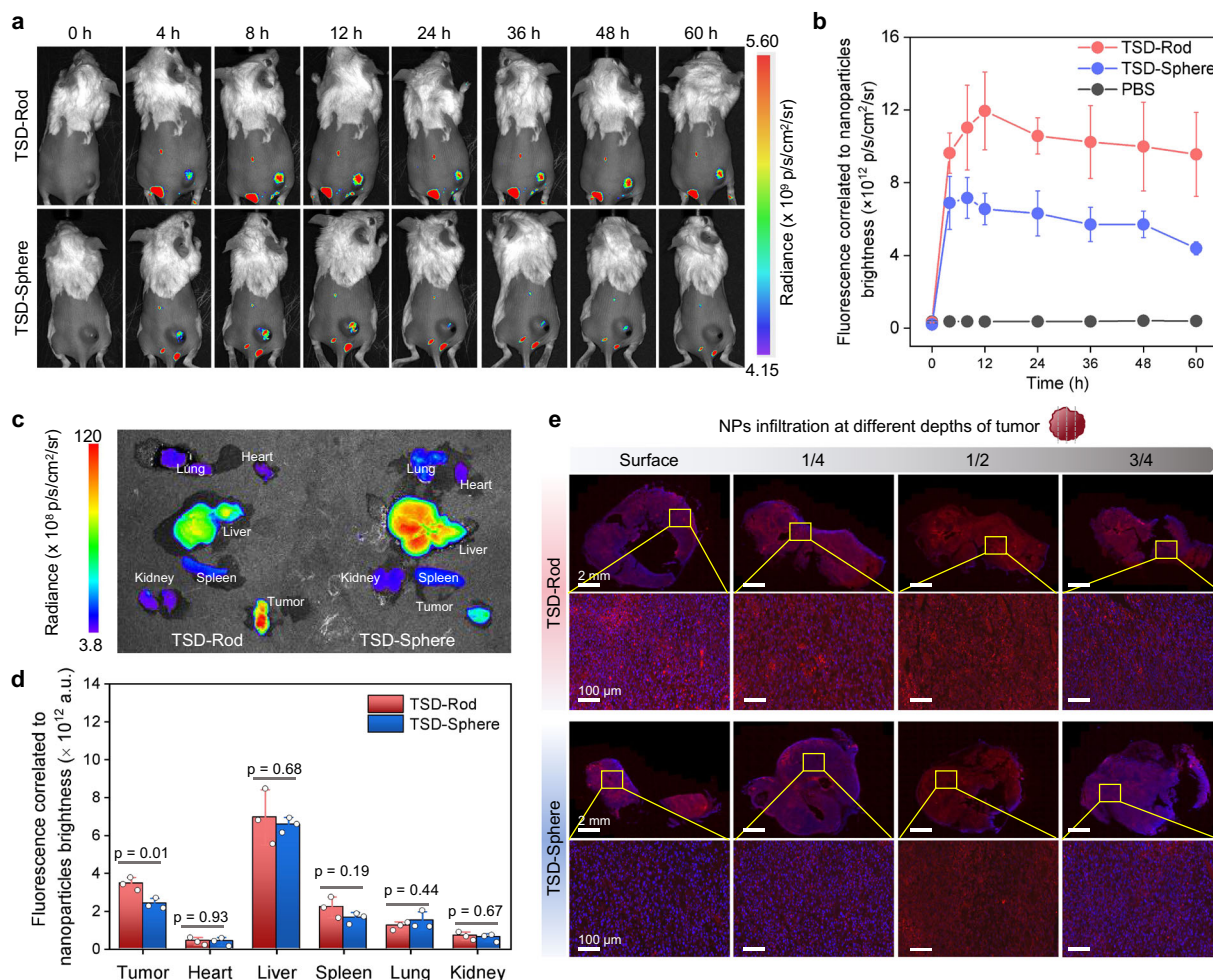


**Fig. 6 | Tumor enrichment and penetration of TSD-Rod and TSD-Sphere.** **a** In vivo near infrared images of tumor enrichment of TSD-Rod/TSD-Sphere. **b** Tumor enrichment profiles of TSD-Rod/TSD-Sphere. Data are presented as mean  $\pm$  SD ( $n = 3$  mice). The intensity of TSD-Sphere was normalized with TSD-Rod to eliminate their fluorescence difference. **c** Ex vivo fluorescence images of organs and tumors at 12 h post injection. **d** Histograms of TSD-Rod/TSD-Sphere distribution in (c). The intensity of TSD-Sphere was normalized with TSD-Rod to eliminate their

fluorescence difference. Data are presented as mean  $\pm$  SD ( $n = 3$  mice). a.u. refers to arbitrary unit. Two-tailed Student's *t* test was performed for comparisons between two groups. A significance level of  $p < 0.05$  was utilized for determining statistical significance. **e** CLSM images of tumor slices at different depths (Scale bar: 2 mm for overview, 100  $\mu$ m for enlarged region) ( $n = 3$  independent experiments). Created in BioRender. Mou, X. (2025) <https://BioRender.com/tflndv>. Source data are provided in Source Data file.

outcomes. With more efforts on elongating  $\pi$ -conjugation, inducing J-aggregation and introducing tumor-targeting ligands, supramolecular nanorods with deeper penetration depth and better tumor-selectivity could be further developed for feasible and practical PDT. Overall, this study provides a conceptual and practical framework for leveraging molecular engineering to optimize photochemical activity, self-assembly morphology and biomedical functionality simultaneously for organic photosensitizers. This H-P-H strategy presents a morphological control for predictably achieving anisotropic self-assembly in small molecules, an area previously dominated by polymeric systems. It also highlights how supramolecular self-assembly fundamentally dictates emergent biological properties (delivery and efficacy) different from their molecules, offering insights in developing functional supramolecular self-assemblies.

## Methods

### Synthesis of TPA-S-DCR

5-(4-(diphenylamino)phenyl)thiophene-2-carbaldehyde (355 mg, 1 mmol), DCR (241 mg, 1 mmol) and sodium acetate (41 mg, 0.5 mmol) were dissolved in 10 mL of acetic acid. The mixture was refluxed at 120  $^{\circ}$ C for 12 h under nitrogen. Then the reaction was stopped by

adding cold distilled water. The obtained red precipitate was filtered off and washed by water. After being dried with anhydrous  $\text{Na}_2\text{SO}_4$ , the bulk solid was further purified by flash column chromatograph (silica gel, ethyl acetate/petroleum ether = 1/20). The dark red product was collected with the yield of about 80%.  $^1\text{H}$  NMR (400 MHz,  $\text{DMSO-d}_6$ ):  $\delta$  8.34 (s, 1H), 7.88 (s, 1H), 7.77–7.64 (m, 3H), 7.59 (s, 2H), 7.56 (s, 1H), 7.54 (s, 2H), 7.46 (d,  $J = 5.7$  Hz, 4H), 7.41–7.28 (m, 4H), 7.15–7.09 (m, 3H), 6.99 (d,  $J = 8.9$  Hz, 1H).  $^{13}\text{C}$  NMR (126 MHz,  $\text{THF-d}_8$ ):  $\delta$  173.10, 172.39, 166.05, 165.78, 154.41, 153.72, 147.91, 137.70, 134.49, 131.60, 130.27, 130.09, 129.61, 128.50, 127.78, 127.05, 124.83, 124.47, 123.21, 113.93, 109.88. HRMS (ESI):  $m/z$  calcd. for  $\text{C}_{35}\text{H}_{22}\text{N}_4\text{OS}_2\text{H}^+$  = 579.1313, found  $m/z$  = 579.1304.

### Sonication-assistant self-assembly

These photosensitizers (0.1 or 1.0 mg) were dissolved in 1 mL THF. The THF solution was then added into ultra-pure water (10 mL). The mixture was treated with 2 min of ultrasonic sonication under probe sonicator (50% amplitude). The mixture was then placed in a fume hood under stirring (200 rpm) overnight for THF evaporation. For TPA-S-DCR, TPA-B-DCR and TPE-S-DCR, spherical and rod-shaped nanoparticles were obtained at initial concentration of 0.1 and 1 mg/mL (in THF solution), respectively.

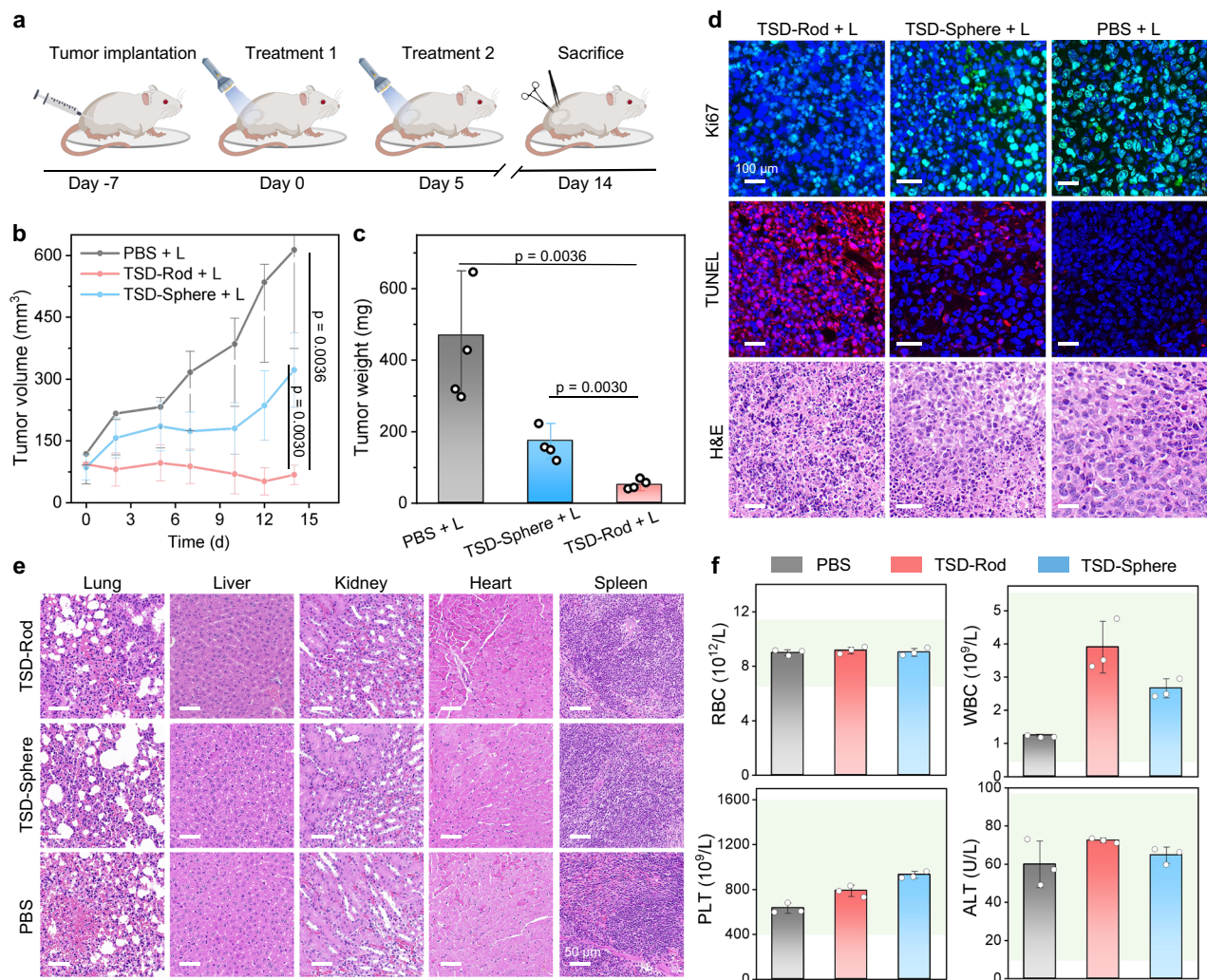


**Fig. 7 | In vivo PDT with TSD-Rod and TSD-Sphere.** **a** Schematic of in vivo PDT procedure. Created in BioRender. Mou, X. (2025) <https://BioRender.com/tf1dnvd>. **b** Tumor volume changes in different group after PDT treatment. Data are presented as mean  $\pm$  SD ( $n = 4$  mice). **c** Tumor weights in these groups, tumors were collected at day 14. Data are presented as mean  $\pm$  SD ( $n = 4$  mice). Two-tailed Student's  $t$  test was performed for comparisons between two groups. A significance level of  $p < 0.05$  was utilized for determining statistical significance. **d** Ki67, TUNEL and H&E staining images of sectioned tumors at day 14 for cell damage evaluation (Scale bar: 100  $\mu$ m). **e** H&E staining images of normal organs after intravenous

injection of TSD-Rod/TSD-Sphere into healthy mice (Scale bar: 50  $\mu$ m). For staining imaging,  $n = 3$  independent experiments. **f** Representative blood routine and biochemistry parameters including red blood cells (RBC, anemia indicator, normal range: 6.50–11.50), white blood cells (WBC, inflammation indicator, normal range: 0.80–10.60), blood platelets (PLT, coagulation indicator, normal range: 400–1600) and alanine aminotransferase (ALT, liver function indicator, normal range: 10.06–96.47) in TSD-Rod/TSD-Sphere-injected healthy mice. The normal ranges of the above indexes of healthy mice were represented in green region. Data are presented as mean  $\pm$  SD ( $n = 3$  mice). Source data are provided in Source Data file.

### ROS generation tests

TSD-Rod and TSD-Sphere were first concentrated to reach a TPA-SDCR concentration of 1mM (detected by UV-vis spectra). DCFH ( $\lambda_{ex} = 480$  nm,  $\lambda_{em} = 525$  nm), DHR123 ( $\lambda_{ex} = 507$  nm,  $\lambda_{em} = 529$  nm), HPF ( $\lambda_{ex} = 480$  nm,  $\lambda_{em} = 514$  nm) and ABDA ( $\lambda_{ab} = 378$  nm) served as the general ROS,  $\bullet O_2$ ,  $\bullet OH$  and  $^1O_2$  generation probes, respectively. The preparation of the testing solution was as follows. To prepare DCFH, DCFH-DA was dissolved in 0.5 mL of EtOH (1 mM), which was further added into 2 mL of NaOH solution (1 mM). After 30 min reaction at room temperature, 7.5 mL of phosphate buffered saline (PBS) solution was then added to obtain DCFH solution (50  $\mu$ M). 1980  $\mu$ L of DCFH solution and 20  $\mu$ L of nanoparticles suspension were mixed in a cuvette. Prior and after white light irradiation (20 mW/cm<sup>2</sup>) for pre-designate time, the mixture was subjected to photoluminescence (PL) spectrum measurement. The working concentrations for DHR123, HPF and ABDA were 20, 10, and 50  $\mu$ M, respectively. The testing concentration of nanoparticles was 10  $\mu$ M (based on photosensitizer molar concentration).

### Ethical statement

All the animal experiments were conducted under the guidance and regulations of the Chinese Law on Institutional Animal Care and Use. And the entire experiment was approved by the Animal Ethics Committee of the South China Agricultural University (Approval ID: 2024D003). Maximal tumor sizes were within permission limits. Mice were housed in a controlled environment maintained at approximately 22  $^{\circ}$ C, with a 12 h light/dark cycle. The relative humidity was maintained at an appropriate level (50%). Standard rodent chow and water were available to ensure the well-being and normal physiological functions of the animals. Mice anesthesia was realized by 1.5% isoflurane inhalation with the small animal gas anesthesia instrument. Mice were euthanized with excessive isoflurane anesthesia.

### Establishment of tumor-bearing mouse model

6 weeks old BALB/c female mice were raised in SPF-level feeding conditions (26  $^{\circ}$ C, humidity of 50%) with adequate food and water.

After hair removal on the back of mice, 4T1 cells ( $2 \times 10^6$ ) suspended in 100  $\mu\text{L}$  PBS were injected subcutaneously into the upper part of the right leg. The tumor volume was measured every two days. Volume =  $0.5 \times (\text{tumor length}) \times (\text{tumor width})^2$ .

### In vivo and ex vivo imaging

When the tumor volumes reached about 90  $\text{mm}^3$ , these 4T1 tumor-bearing mice were randomly divided into three groups ( $n = 3$  mice for each group): TSD-Rod, TSD-Sphere and PBS. 100  $\mu\text{L}$  isotonic solution of TSD-Rod (750  $\mu\text{g}/\text{mL}$ ), TSD-Sphere (750  $\mu\text{g}/\text{mL}$ ) and PBS were intravenously injected through tail vein. The living imaging system recorded the fluorescence signal at 0, 4, 8, 12, 24, 36, 48 and 60 h post injection. Another 12 mice were (6 for TSD-Rod and 6 for TSD-Sphere) subjected for ex vivo organ imaging. Similar injection dosage was employed. At 8 h and 12 h post injection, the mice were sacrificed and dissected. The heart, liver, spleen, lung, kidney and tumor were collected and imaged. To study the tumor penetration ability, the tumors collected at 8 h were sliced at different depths. The slices at tumor surface, 1/4, 1/2 and 3/4 depth were stained with DAPI (2  $\mu\text{g}/\text{mL}$ ) and further imaged with CLSM.

### In vivo PDT

The 4T1 tumor-bearing mice were randomly divided into 6 groups ( $n = 4$  mice for each group): PBS, PBS + Light (L), TSD-Rod, TSD-Rod + L, TSD-Sphere, TSD-Sphere + L. On day 0, TSD-Rod, TSD-Sphere and PBS. 200  $\mu\text{L}$  isotonic solution of TSD-Rod (750  $\mu\text{g}/\text{mL}$ ), TSD-Sphere (750  $\mu\text{g}/\text{mL}$ ) and PBS were intravenously injected through tail vein. At 8 h post-injection, the mice were anesthetized with isoflurane and the tumors in light groups were exposed to light irradiation for 30 min (100  $\text{mW}/\text{cm}^2$ ). Similar nanoparticle injection and light treatment procedures were repeated on day 5. During the entire treatment, the tumors sizes were measured every 2 days. On day 14, the mice were sacrificed and dissected. The tumors were excised, weighed and further stained with H&E, TUNEL and Ki67 for histological analysis.

### Biosafety evaluation

The normal organs from these mice were also collected for H&E staining. To further study the biosafety of TSD-Rod and TSD-Sphere, 9 healthy mice were divided into three groups ( $n = 3$  mice for each group): TSD-Rod, TSD-Sphere and PBS. TSD-Rod, TSD-Sphere and PBS. 200  $\mu\text{L}$  isotonic solution of TSD-Rod (750  $\mu\text{g}/\text{mL}$ ), TSD-Sphere (750  $\mu\text{g}/\text{mL}$ ) and PBS were intravenously injected through tail vein. After 9 days, blood routine and blood biochemical tests were conducted.

### Statistics and reproducibility

Origin2018 software was used for statistical analysis, curve smoothing, graphic embellishment, linear and exponential fitting of correlation curves of light scattering results. AFM images height information was analyzed and derived from NanoScope Analysis 1.8 software. Quantitative comparison of fluorescence intensity in CLSM was carried out by ImageJ software. All experiments were conducted with at least three independent replicates. Quantitative data were shown as mean  $\pm$  standard deviation (SD) with  $n \geq 3$ . Statistical analysis between two groups of dataset experiments was compared using a two-tailed Student's *t*-test. A significance level of  $p < 0.05$  was utilized for determining statistical significance.

### Reporting summary

Further information on research design is available in the Nature Portfolio Reporting Summary linked to this article.

## Data availability

All data that support the findings of this work are available within the paper, the Supplementary Information files and from corresponding author(s) upon request. Source data are provided with this paper.

## References

1. Obaid, G. et al. Engineering photodynamics for treatment, priming and imaging. *Nat. Rev. Bioeng.* **2**, 752–769 (2024).
2. Juarranz, Á, Jaén, P., Sanz-Rodríguez, F., Cuevas, J. & González, S. Photodynamic therapy of cancer. Basic principles and applications. *Clin. Transl. Oncol.* **10**, 148–154 (2008).
3. Dolmans, D. E. J. G., Fukumura, D. & Jain, R. K. Photodynamic therapy for cancer. *Nat. Rev. Cancer* **3**, 380–387 (2003).
4. Pham, T. C., Nguyen, V., Choi, Y., Lee, S. & Yoon, J. Recent Strategies to Develop Innovative Photosensitizers for Enhanced Photodynamic Therapy. *Chem. Rev.* **121**, 13454–13619 (2021).
5. Li, B., Lu, L., Zhao, M., Lei, Z. & Zhang, F. An efficient 1064 nm NIR-II excitation fluorescent molecular dye for deep-tissue high-resolution dynamic bioimaging. *Angew. Chem. Int. Ed.* **57**, 7483–7487 (2018).
6. Liu, S. et al. Cationization-enhanced Type I and Type II ROS generation for photodynamic treatment of drug-resistant bacteria. *ACS Nano* **16**, 9130–9141 (2022).
7. Zhao, D. et al. Atomic-iodine-substituted polydiacetylene nanospheres with boosted intersystem crossing and nonradiative transition through complete radiative transition blockade for ultraeffective phototherapy. *Aggregate* **5**, e576 (2024).
8. Chen, P. et al. Bandgap modulation and lipid intercalation generates ultrabright D–A–D-Based Zwitterionic small-molecule nanoagent for precise NIR-II excitation phototheranostic applications. *Adv. Funct. Mater.* **32**, 2208463 (2022).
9. Xiong, T., Chen, Y., Li, M., Chen, X. & Peng, X. Recent progress of molecular design in organic type I photosensitizers. *Small* **21**, 2501911 (2025).
10. Feng, G., Zhang, G. & Ding, D. Design of superior phototheranostic agents guided by Jablonski diagrams. *Chem. Soc. Rev.* **49**, 8179–8234 (2020).
11. Chen, C., Ou, H., Liu, R. & Ding, D. Regulating the photophysical property of organic/polymer optical agents for promoted cancer phototheranostics. *Adv. Mater.* **32**, 1806331 (2020).
12. Xiong, X. et al. Self-assembly strategies of organic small-molecule photosensitizers for photodynamic therapy. *Coord. Chem. Rev.* **510**, 215863 (2024).
13. Marcon, R. O. & Brochsztain, S. Aggregation of 3,4,9,10-Perylene-1,10-dione radical anions and dianions generated by reduction with dithionite in aqueous solutions. *J. Phys. Chem. A* **113**, 1747–1752 (2009).
14. Görl, D., Zhang, X. & Würthner, F. Molecular assemblies of perylene bisimide dyes in water. *Angew. Chem. Int. Ed.* **51**, 6328–6348 (2012).
15. Sun, H. et al. Suppressing ACQ of molecular photosensitizers by distorting the conjugated-plane for enhanced tumor photodynamic therapy. *Chem. Sci.* **15**, 940–952 (2024).
16. Li, Z. et al. Activatable nano-photosensitizers for precise photodynamic cancer therapy. *Coord. Chem. Rev.* **493**, 215324 (2023).
17. Almeida, H., Traverso, G., Sarmiento, B. & Das Neves, J. Nanoscale anisotropy for biomedical applications. *Nat. Rev. Bioeng.* **2**, 609–625 (2024).
18. Chan, W. C. W. Principles of nanoparticle delivery to solid tumors. *BME Front.* **4**, 16 (2023).
19. Barua, S. & Mitragotri, S. Challenges associated with penetration of nanoparticles across cell and tissue barriers: a review of current status and future prospects. *Nano Today* **9**, 223–243 (2014).

20. Iyer, A. K., Khaled, G., Fang, J. & Maeda, H. Exploiting the enhanced permeability and retention effect for tumor targeting. *Drug Discov. Today* **11**, 812–818 (2006).
21. Maeda, H., Tsukigawa, K. & Fang, J. A Retrospective 30 Years after discovery of the enhanced permeability and retention effect of solid tumors: next-generation chemotherapeutics and photodynamic therapy—problems, solutions, and prospects. *Microcirculation* **23**, 173–182 (2016).
22. Manno, M., Bongiovanni, A., Margolis, L., Bergese, P. & Arosio, P. The physico-chemical landscape of extracellular vesicles. *Nat. Rev. Bioeng.* **3**, 68–82 (2025).
23. Miao, D. et al. Photothermal nanofiber-mediated photoporation for gentle and efficient intracellular delivery of macromolecules. *Nat. Protoc.* **20**, 1810–1845 (2025).
24. Bariwal, J., Ma, H., Altenberg, G. A. & Liang, H. Nanodiscs: a versatile nanocarrier platform for cancer diagnosis and treatment. *Chem. Soc. Rev.* **51**, 1702–1728 (2022).
25. Chen, Z. et al. Nanobowl-supported liposomes improve drug loading and delivery. *Nano Lett.* **20**, 4177–4187 (2020).
26. Cong, V. T. et al. Can the shape of nanoparticles enable the targeting to cancer cells over healthy cells?. *Adv. Funct. Mater.* **31**, 2007880 (2021).
27. Xu, R. et al. Less is more: Asymmetric D–A type agent to achieve dynamic self-assembled nanoaggregates for long-acting photodynamic therapy. *Adv. Mater.* **36**, 2402434 (2024).
28. Yu, Q. et al. Rodlike block copolymer micelles of controlled length in water designed for biomedical applications. *Macromolecules* **52**, 5231–5244 (2019).
29. Wang, M. et al. Morphology tuning of aggregation-induced emission probes by flash nanoprecipitation: shape and size effects on in vivo imaging. *ACS Appl. Mater. Interfaces* **10**, 25186–25193 (2018).
30. Zhang, J., Xu, B., Tian, W. & Xie, Z. Tailoring the morphology of AIEgen fluorescent nanoparticles for optimal cellular uptake and imaging efficacy. *Chem. Sci.* **9**, 2620–2627 (2018).
31. Tang, Y., Xiang, D. & Li, Q. In situ secondary self-assembly of near-infrared II J-aggregates: a novel phototheranostic strategy for inducing tumor pyroptosis. *Adv. Mater.* **37**, 2501184 (2025).
32. Liu, Y. et al. In situ self-assembled J-aggregate nanofibers of glycosylated Aza-BODIPY for Synergetic cell membrane disruption and type I photodynamic therapy. *Angew. Chem. Int. Ed.* **62**, e202309786 (2023).
33. Han, K. et al. Tumor-triggered geometrical shape switch of chimeric peptide for enhanced in vivo tumor internalization and photodynamic therapy. *ACS Nano* **11**, 3178–3188 (2017).
34. Hua, Z. et al. Anisotropic polymer nanoparticles with controlled dimensions from the morphological transformation of isotropic seeds. *Nat. Commun.* **10**, 5406 (2019).
35. Oliver, A. M. et al. Scalable fiber-like micelles and block Co-micelles by polymerization-induced crystallization-driven self-assembly. *J. Am. Chem. Soc.* **140**, 18104–18114 (2018).
36. Su, W. et al. Porphyrin-assembled nano-photosensitizer with near-infrared response for highly efficient type I photodynamic and photothermal therapy. *Sci. China Mater.* **68**, 2122–2131 (2025).
37. Liu, H., Li, X., Li, X. & Huang, J. Nanostructured self-assemblies of photosensitive dyes: green and efficient theranostic approaches. *Green. Chem. Eng.* **4**, 399–416 (2023).
38. Yang, Y., Li, Q. & Li, Z. Advances in organic room-temperature phosphorescence: design strategies, photophysical mechanisms, and emerging applications. *Mater. Chem. Front.* **9**, 744–753 (2025).
39. Fateminia, S. M. A. et al. Simultaneous increase in brightness and singlet oxygen generation of an organic photosensitizer by nano-crystallization. *Small* **14**, 1803325 (2018).
40. Hu, X. et al. J-aggregation strategy toward potentiated NIR-II fluorescence bioimaging of molecular fluorophores. *Adv. Mater.* **36**, 2304848 (2024).
41. Mei, J., Leung, N. L. C., Kwok, R. T. K., Lam, J. W. Y. & Tang, B. Z. Aggregation-induced emission: together we shine, united we soar!. *Chem. Rev.* **115**, 11718–11940 (2015).
42. Ma, S. et al. Organic molecular aggregates: from aggregation structure to emission property. *Aggregate* **2**, e96 (2021).
43. Tu, Y., Zhao, Z., Lam, J. W. Y. & Tang, B. Z. Mechanistic connotations of restriction of intramolecular motions (RIM). *Natl. Sci. Rev.* **8**, a260 (2021).
44. Liu, S. et al. Morphology-controlled long-range photogenerated charge carrier transfer pathway for enhanced photocatalytic hydrogen production. *Nano Lett.* **25**, 4596–4604 (2025).
45. Zhang, X., Chen, Z. & Würthner, F. Morphology control of fluorescent nanoaggregates by co-self-assembly of wedge- and dumbbell-shaped amphiphilic perylene bisimides. *J. Am. Chem. Soc.* **129**, 4886–4887 (2007).
46. Zhang, X., Görl, D., Stepanenko, V. & Würthner, F. Hierarchical growth of fluorescent dye aggregates in water by fusion of segmented nanostructures. *Angew. Chem. Int. Ed.* **53**, 1270–1274 (2014).
47. Chen, L. et al. Complexity made easy: aggregation-induced emission small molecules for cancer diagnosis and phototherapies. *Aggregate* **5**, e657 (2024).
48. Wang, H. et al. Aggregation-Induced Emission (AIE), life and health. *ACS Nano* **17**, 14347–14405 (2023).
49. Gruschwitz, F. V., Klein, T., Catrouillet, S. & Brendel, J. C. Supramolecular polymer bottlebrushes. *Chem. Commun.* **56**, 5079–5110 (2020).
50. Zhu, Y. et al. Self-assembling peptide with dual function of cell penetration and antibacterial as a nano weapon to combat intracellular bacteria. *Sci. Adv.* **11**, s3844 (2025).
51. Kim, J. et al. In situ self-assembly for cancer therapy and imaging. *Nat. Rev. Mater.* **8**, 710–725 (2023).
52. Hou, Y. et al. Insights into the isomeric effect on the self-assembly of donor-acceptor type aggregation-induced emission luminogens: colour-tuning and shape-controlling. *J. Lumin.* **204**, 221–229 (2018).
53. Shao, A. et al. Far-red and near-IR AIE-active fluorescent organic nanoprobe with enhanced tumor-targeting efficacy: shape-specific effects. *Angew. Chem. Int. Ed.* **54**, 7275–7280 (2015).
54. Dang, D. et al. 1 + 1 » 2: dramatically enhancing the emission efficiency of TPE-Based AIEgens but keeping their emission color through tailored alkyl linkages. *Adv. Funct. Mater.* **28**, 1707210 (2018).
55. Balakrishnan, K. et al. Effect of side-chain substituents on self-assembly of perylene diimide molecules: morphology control. *J. Am. Chem. Soc.* **128**, 7390–7398 (2006).
56. Gui, Y. et al. Thiophene  $\pi$ -bridge manipulation of NIR-II AIEgens for multimodal tumor phototheranostics. *Angew. Chem. Int. Ed.* **63**, e202318609 (2024).
57. Hu, Z. et al. Engineering long-lived charge separation states boosts type-I ROS generation for efficient cancer therapy. *Biomaterials* **319**, 123218 (2025).
58. Zhu, Y. et al. Acceptor elongation boosted intersystem crossing affords efficient NIR Type-I and AIE-Active photosensitizers for targeting ferroptosis-based cancer therapy. *Adv. Healthc. Mater.* **14**, 2404505 (2025).
59. Lepeltier, E., Bourgaux, C. & Couvreur, P. Nanoprecipitation and the “Ouzo effect”: application to drug delivery devices. *Adv. Drug Deliv. Rev.* **71**, 86–97 (2014).
60. Feng, G. et al. Polymeric nanorods with aggregation-induced emission characteristics for enhanced cancer targeting and imaging. *Nanoscale* **10**, 5869–5874 (2018).
61. Wang, Y. et al. Dual enhancement of phosphorescence and circularly polarized luminescence through entropically driven self-assembly of a Platinum(II) complex. *Angew. Chem. Int. Ed.* **63**, e202403898 (2024).

62. Zhang, X. et al. The entropy-controlled strategy in self-assembling systems. *Chem. Soc. Rev.* **52**, 6806–6837 (2023).
63. Horn, D. & Rieger, J. Organic nanoparticles in the aqueous phase—theory, experiment, and use. *Angew. Chem. Int. Ed.* **40**, 4330–4361 (2001).
64. Cabral, H., Miyata, K., Osada, K. & Kataoka, K. Block copolymer micelles in nanomedicine applications. *Chem. Rev.* **118**, 6844–6892 (2018).
65. Jiang, L., Zhou, S., Zhang, X., Wu, W. & Jiang, X. Dendrimer-based nanoparticles in cancer chemotherapy and gene therapy. *Sci. China Mater.* **61**, 1404–1419 (2018).
66. Yu, M. et al. Rotation-facilitated rapid transport of nanorods in mucosal tissues. *Nano Lett.* **16**, 7176–7182 (2016).
67. Wang, Y. et al. Spatiotemporal tracing of the cellular internalization process of rod-shaped nanostructures. *ACS Nano* **16**, 4059–4071 (2022).
68. Adriani, G. et al. The preferential targeting of the diseased microvasculature by disk-like particles. *Biomaterials* **33**, 5504–5513 (2012).
69. Cong, V. T. et al. How can we use the endocytosis pathways to design nanoparticle drug-delivery vehicles to target cancer cells over healthy cells?. *Chem. Soc. Rev.* **51**, 7531–7559 (2022).
70. Xu, Z. et al. Facet-Dependent Biodegradable Mn<sub>3</sub>O<sub>4</sub> nanoparticles for ameliorating Parkinson's disease. *Adv. Healthc. Mater.* **10**, 2101316 (2021).
71. Wang, P. et al. Visualization of the cellular uptake and trafficking of DNA origami nanostructures in cancer cells. *J. Am. Chem. Soc.* **140**, 2478–2484 (2018).
- performed in vivo experiments; Q.Y.T. and G.F. Analyzed the data and drafted the manuscripts. All the authors provided comments on manuscript.

### Competing interests

The authors declare no competing interests.

### Additional information

**Supplementary information** The online version contains supplementary material available at <https://doi.org/10.1038/s41467-025-66470-9>.

**Correspondence** and requests for materials should be addressed to Guangxue Feng.

**Peer review information** *Nature Communications* thanks anonymous reviewer(s) for their contribution to the peer review of this work. [A peer review file is available.]

**Reprints and permissions information** is available at <http://www.nature.com/reprints>

**Publisher's note** Springer Nature remains neutral with regard to jurisdictional claims in published maps and institutional affiliations.

**Open Access** This article is licensed under a Creative Commons Attribution-NonCommercial-NoDerivatives 4.0 International License, which permits any non-commercial use, sharing, distribution and reproduction in any medium or format, as long as you give appropriate credit to the original author(s) and the source, provide a link to the Creative Commons licence, and indicate if you modified the licensed material. You do not have permission under this licence to share adapted material derived from this article or parts of it. The images or other third party material in this article are included in the article's Creative Commons licence, unless indicated otherwise in a credit line to the material. If material is not included in the article's Creative Commons licence and your intended use is not permitted by statutory regulation or exceeds the permitted use, you will need to obtain permission directly from the copyright holder. To view a copy of this licence, visit <http://creativecommons.org/licenses/by-nc-nd/4.0/>.

© The Author(s) 2025

### Acknowledgements

This work was financially supported by National Key R&D Program of China (2024YFA1307601) (G.F.), National Natural Science Foundation of China (52473300, 22205067) (G.F.), Key-Area Research and Development Program of Guangdong Province (2024B0101040001) (G.F. and B.Z.T.), Guangdong Provincial Key Laboratory of Luminescence from Molecular Aggregates (2023B1212060003) (G.F.), Guangdong Basic and Applied Basic Research Foundation (2023B1515040003) (G.F.).

### Author contributions

Q.Y.T. and G.F. conceived the study; B.Z.T. provided guidance and suggestions. Q.Y.T. performed chemical synthesis, nanoparticle fabrication and in vitro characterization; Y.L. synthesized TPA-S-IC; H.Y.J. performed simulation; B.H.X. helped light scattering testing and analysis; Q.Y.T.